Magnetic Fe_{2-x}Ni_xP (x = 0.6-0.7) Aerogels Prepared from Nanoparticle Assembly: The Functional Whole is the Sum of its Parts

Malsha A. Hettiarachchi, 1,† Tepora Su'a, 1,† Ali-hamza Ramzan, 1 Shiva Pokhrel, 2 Boris

Nadgorny, 2 Stephanie L. Brock 1,*

¹Department of Chemistry, Wayne State University, Detroit, MI, 48202 USA

²Department of Physics and Astronomy, Wayne State University, Detroit, MI 48201, USA

[†]These authors contributed equally to the work

Abstract

Three-dimensional magnetic Fe_{2-x}Ni_xP (x = 0.6-0.7) nanorod assemblies (gels and aerogels) were prepared by oxidation of Fe_{2-x}Ni_xP nanorods capped with 11-mercaptoundecanoic acid (MUA) and 1-dodecanthiol (DDT) and their magnetic properties were evaluated in comparison to discrete nanorod precursors, and in the context of the interfacial chemical characteristics associated with the ligand group employed. Treatment of MUA- and DDT-capped Fe_{2-x}Ni_xP nanorods with hydrogen peroxide results in gels that largely retain the structural (as assessed by powder X-ray diffraction) and morphological (as revealed by transmission electron microscopy) features of the nanorods in a pore-matter integrated network. However, aerogels created from MUA-capped particles undergo dispersion upon treatment with ethylenediaminetetraacetic acid (EDTA), whereas those produced from DDT-capped particles remain unchanged. Likewise, reductive annealing resulted in cleavage of the aerogel produced from DDT-capped particles, whereas the aerogels produced from MUA-capped particles remained intact, if more compact, as reflected in a ca. 50% decrease in surface area. The data are consistent with distinct interfacial chemistry in the two networks: amorphous phosphite/phosphate olation linkages in aerogels produced from DDT-

capped particles vs. a combination of phosphite/phosphate olation linkages and metal-ion crosslinking of pendant carboxylates in aerogels produced from MUA-capped particles. The superparamagnetic blocking temperature (T_B) of discrete Fe_{2-x}Ni_xP nanoparticles, and the aerogels made from 11-MUA and 1-DDT exchanged nanoparticles, all appear in the range of 30-40 K and the field dependent magnetization profiles (M-H) exhibit minimal hysteresis at 50 K with coercivity (H_C) values ~10 Oe. Thus, the Fe_{2-x}Ni_xP nanoparticles comprising the aerogel network behave independently, as expected for a disordered 3-D assembly, and the magnetic aerogels can be regarded as a summation of their individual components.

Introduction

Fe_{2-x}Ni_xP materials have been extensively studied due to their interesting composition dependent catalytic ¹⁻⁵ and magnetic properties. ⁶⁻⁸ In addition to promise for hydro-treating and electrocatalytic water splitting, these phases are also potential candidates for application in magnetic refrigeration (MR), an efficient and environmentally friendly solid state cooling technology alternative. MR relies on materials that exhibit a large magnetocaloric effect, in which a change in temperature manifests when transitioning between magnetic states, typically at the Curie temperature, T_C. ⁹ For practical applications, low thermal and magnetic hysteresis is also important for efficient refrigeration cycling, as is a large surface area for contact with the heat transfer fluid, and mechanical stability, ^{10, 11} all of which can be achieved by appropriate introduction of porosity and attention to micro/ nanostructure. ¹²⁻¹⁵ One approach to the design of functional magnetic refrigeration materials is thus to start with discrete nanoparticles compositionally tuned to maximize the magnetocaloric effect in the temperature range of interest, and exploit suitable assembly processes to form the desired architectures. ¹⁶⁻²¹

The formation of integrated nanostructures by assembly of discrete nanoparticles is a topic of current critical interest. 18, 22-31 Previously, we and others have demonstrated that colloids of metal chalcogenide^{24, 26, 28-38} and metal phosphides^{39, 40} can undergo self-assembly into porous networks by different processes, including: (1) metal ion crosslinking of pendant chelating functionalities on the surface terminating ligands, and (2) oxidative stripping of surface terminating ligands followed by oxidative crosslinking of particles (Figure 1). Note that the first process is agnostic with respect to nanoparticle identity, predicated only on having a robust surface linkage and appropriate termination to enable metal cation crosslinking. The second process depends on having oxidatively susceptible surface groups (such as thiolates) or ligand stripped surfaces, and on the redox characteristics of the non-metal (chalcogenide or phosphide). Notably, the redox characteristics of chalcogenides (Q²-) enables formation of di-chalcogenide crosslinkers, $2Q^{2-} \rightarrow Q_2^{2-} + 2e^-$, with modest oxidants, such as H_2O_2 , although formation of QO_3^{2-} or QO_4^{2-} type species becomes more prevalent as Q becomes heavier (more electropositive; Te>Se>S). Formation of chalcogenite(ate) can be largely avoided with the use of non-oxygen transferring oxidants, such as tetranitromethane (TNM). However, the analogous phosphide to di-phosphide reaction: $2P^{3-} \rightarrow P_2^{4-} + 2e^{-}$ is considerably more challenging, and oxidative assembly of phosphides does not occur with TNM, proceeding in the presence of H₂O₂ via formation of surface phosphite/ate followed by olation. It is worth noting that oxidative crosslinking and metal-ion crosslinking can be attained in the same assembly even without the introduction of an external crosslinking cation. This occurs when oxidative assembly is performed on systems with ligands featuring pendant chelating functionalities. Specifically, oxidation of surface ligands exposes metal ions, which, when liberated by solvation, can crosslink particles via remaining bound

ligands. This competitive metal-ion crosslinking assembly process can be avoided by eschewing ligands with pendant chelates (e.g., by using dodecanthiolate in lieu of mercaptoundecanoic acid).

In the present work, we seek to prepare porous and disordered assemblies of magnetic transition metal phosphides with characteristics suitable for magnetic refrigeration. We seek to understand whether the linking chemistry in a fractal structure affects the magnetic properties of the assembly, particularly with respect to the nature of the interfaces, when compared to discrete (unlinked) nanoparticle powders. Pileni and co-workers were the first to show experimentally that the magnetic behavior of 3-D ordered magnetic nanoparticle assemblies is distinct from disordered assemblies, but these changes are subtle.^{16, 19} Accordingly, we expect that the magnetic phosphide gel structures will behave as independently interacting particles.

We have selected as our synthetic target Fe_{1.2}Ni_{0.8}P nanoparticles for the following reasons: (1) pnictides adopting the Fe₂P structure-type are known to exhibit significant magnetocaloric properties (most notably, MnFeP_{0.5}As_{0.5}⁴¹); (2) Fe_{2-x}Ni_xP has a compositionally tunable T_C ranging on the low end from <100 K (x = 1) to 342 K on the high end (x =0.14), meaning some compositions are suitable for near room-temperature refrigeration applications, but by the same token, Fe_{1.2}Ni_{0.8}P has a T_C = 125 K,⁷ making it straightforward to perform routine magnetic characterization in-house, without having to resort to high-temperature (>300K) measurements; (3) Fe_{2-x}Ni_xP nanoparticles tend to adopt a rod-shaped morphology, which has been correlated (in related CdSe nanorods) to mechanically stronger gels than spherical nanoparticles;³⁵ and (4) we have previously reported assembly of Ni₂P nanoparticles, and therefore have reasonable expectation of success in transitioning to ternary Fe_{2-x}Ni_xP.⁴⁰

Here we report the synthesis of magnetic Fe_{2-x}Ni_xP aerogels, targeting x = 0.8, but realizing x = 0.7, prepared from nanorods of three different aspect ratios. The magnetic properties of the Fe_{2-x}Ni_xP aerogels formed with nanoparticles functionalized with 1-dodecanethiol (phosphite/atelinked only) and 11-mercaptoundecanoic acid (phosphite/ate linked + metal-ion-linked via pendant carboxylate) are reported and their behavior relative to the individual nanoparticles is discussed. We note that the majority of magnetic aerogels known to date are composites of magnetic components folded into non-magnetic oxides, carbon, or polymers.⁴² While single-phase oxide-based magnetic aerogels are documented, ⁴³⁻⁴⁶ and a magnetic aerogel based on gadolinium phosphate was recently reported, ⁴⁷ the present work represents the first example, to the best of our knowledge, of a phosphide-based magnetic aerogel. ⁴²

Methods

Reagents:

Nickel(II) acetylacetonate (Ni(acac)₂, 95%, Alfa Aesar), trioctylphosphine (TOP, 98%, Strem), Iron(0) pentacarbonyl (Fe(CO)₅, 99.99%, Sigma-Aldrich), oleylamine (C₁₈ content of 80–90%, Acros), octyl ether (90%, TCI America), chloroform (99.9%, Fisher), 11-mercaptoundecanoic acid (MUA, 95%, Aldrich), tetramethylammonium hydroxide pentahydrate (TMAH, 99%, Acros), dodecanethiol (≥98%, Aldrich), hydrogen peroxide (H₂O₂, 3 and 30% in water, Fisher), tetranitromethane (TNM, Sigma-Aldrich), triethylamine (TEA, technical grade, Strem), absolute ethanol (AAPER Alcohols and Chemicals), acetone (Fisher), hexane (Fisher), ethylenediamine tetraacetic acid disodium salt dihydrate (EDTA, Fisher) and ethyl acetate (99.9%, Fisher) were used as received.

Synthesis of Fe_{2-x}Ni_xP Nanoparticles

Nanoparticles of Fe_{2-x}Ni_xP were synthesized as previously described, targeting x = 0.8.⁷ Briefly, a mixture of Ni(acac)₂ (0.8 mmol), oleylamine (1-2 mL), octylether (10 mL), and TOP (3-5 mL) was degassed and heated to 230 °C to yield a black solution comprising amorphous Ni-P particles. Fe(CO)₅ (1.2 mmol) was then added and the contents were further heated at 230 °C for another 30 min to yield Ni-Fe-P amorphous particles. To encourage crystallization, the temperature was increased to 350 °C for 10 h.

Thiolate Exchange of Ternary Phosphide Nanoparticles

Surface ligand exchange of as-prepared batches of Fe_{2-x}Ni_xP was carried out using 11-MUA or 1-DDT in a 1:4 metal to ligand ratio following the reported procedures for InP and Ni₂P nanoparticles, respectively.^{39, 40} The amount of ligand required was estimated by the formula weight of the corresponding nanoparticles, assuming no contribution by the surface ligands (oleylamine or TOP) towards the mass of the product.

Wet Gel and Aerogel Formation

Batches of ligand-exchanged Fe_{2-x}Ni_xP nanoparticles were subjected to oxidation-induced gelation using 3% H₂O₂. The 11-MUA and 1-DDT capped nanoparticles were dispersed in absolute ethanol (3-5 mL), and hexane/acetone (1:1 v/v) (3-5 mL) solvent mixture, respectively, in a polyethylene vial. An aqueous solution of 3% H₂O₂ (65-100 μL) was added into this dispersion, and the vial was briefly agitated. The gelation starts in 11-MUA exchanged nanoparticles in approximately 30 min, while the gelation of 1-DDT capped nanoparticles can be observed after about 12 h. The gels were aged in the mother liquor for about 14 days. After aging, the gel solvent was carefully exchanged ten times with 3-5 mL of acetone over the course of 2 days. The resultant wet gels were then supercritically dried using a SPI-DRY CO₂ critical point dryer equipped with an ISOTEMP 10065 water bath set at 18°C. The plastic cap of the

polyethylene vial containing the wet gel sample was punctured with a needle multiple times and the entire vial was loaded into the chamber. The chamber was then completely filled with acetone and sealed tightly. Solvent exchange with liquid CO₂ was then carried out in 20 min intervals, over the course of 4 h. For the supercritical drying step, the liquid CO₂ level was drained halfway and the temperature was increased to 37°C. Due to the increase in temperature, the pressure within the chamber reached 89-109 atm allowing CO₂ to obtain the supercritical state. The sample was maintained at the described temperature and pressure for 30 min and then the pressure was slowly relieved to 1 atm over 20 min to isolate the aerogel. The vial was carefully removed, the plastic caps were replaced, and the vials were stored in vacuum desiccators under ambient conditions.

Effect of EDTA treatment on the Fe2-xNixP gel network

The effect of EDTA towards the synthesized Fe_{2-x}Ni_xP gel network was tested analogous to a previously published procedure.²² Briefly, the synthesized aerogel monoliths were redissolved back into their colloidal forms using an aliquot (4 mL) of 0.5 M aqueous EDTA solution at pH 12 by adding drop-wise to the aerogels (Fe_{2-x}Ni_xP +11-MUA and Fe_{2-x}Ni_xP +1-DDT) with brief agitation. The number of moles of EDTA added, was maintained equal to the total number of metal ions in target composition (2 mmol).

Characterization

Powder X-ray diffraction (PXRD). A Bruker Phaser II model X-ray diffractometer equipped with a Cu anode was employed to acquire diffraction patterns in the range $2\Theta = 20 - 70^{\circ}$. Dried nanoparticle and aerogel samples were loaded onto a zero-background quartz sample holder for all measurements.

Transmission Electron Microscopy (TEM). A JEOL 2010 transmission electron microscope operating at 200 kV was employed to obtain all TEM micrographs. The aerogel and nanoparticle

samples were prepared by dispersing the solid sample in hexane followed by sonication and dispersion on a 200 mesh copper grid coated with carbon. An EDAX detector unit attached to the JEOL 2010 was used to carry out the Energy Dispersive Spectroscopy (EDS) measurements to probe composition.

Surface Area Analysis and Porosimetry. A Micromeritics TriStar II 3020 surface area analyzer was used to measure the surface area and analyze the pore size of powdered aerogels samples. The surface areas were obtained by applying the Brunauer–Emmett–Teller (BET) model to nitrogen adsorption/ desorption isotherms acquired at 77 K.. Samples (*ca.* 50 mg) were degassed at 120 °C for 14 h prior to the analysis.

X-Ray Fluorescence Spectrometry. The elemental compositions of Fe, Ni, and P were analyzed with a SHIMADZU EDX-7000 energy dispersive X-Ray Fluorescence Spectrometer (XRF), using PCEDX-Navi software, operating in air with the collimator size of 10 mm. The X-ray generator had a Rhodium target fixed at 50 kV (Rh 50) operating under a 26 μA current, coupled with a silicon drift detector. Solid samples were placed in the middle of a Mylar® cup, which was then placed on the beam window located on the sample plate before characterization.

Inductively Coupled Plasma – Mass Spectrometry. Moles of Fe and Ni in the NPs, MUA AG, and DDT AG samples were obtained using an Agilent 7700x Series Inductively Coupled Plasma – Mass Spectrometer (ICP-MS). Solid powders of the samples (~1.10 mg) were completely dissolved in concentrated nitric acid (2 mL). A 10uL aliquot was retrieved and further diluted by mass to 50.0mL with 2% HNO₃ acid. 2% HNO₃ acid served as the blank solution. In order to calibrate the instrument, Fe and Ni standard solutions (5, 10, 25, 50, 100, 150, 200 ppb) were prepared by serial dilution of a Fe and Ni stock solution.

X-Ray Photoelectron Spectroscopy. High resolution XPS spectra were collected for the NPs and AGs on a NEXSA, ThermoFisher Scientific instrument equipped with a monochromatic Al Kα (1486.7 eV) X-ray Source operating at 6 mA and 12 kV. Using a spot size of 400μm, the instrument work function was calibrated to give a binding energy of 83.98 eV for Au4f7/2. High resolution scans after 45s Ar sputtering, were collected for the P 2p peak over the range from 125-140eV. The binding energy ranges were shifted using the adventitious C 1s peak at 284.8 eV.

Magnetometry. Magnetic measurements were acquired on dried aerogel and nanoparticle powders (stored under an inert atmosphere). A Quantum Design PPMS 6000 system was used to record the temperature-dependent DC magnetization data, Zero-Field Cooling (ZFC) and Field Cooling (FC), under a 100 Oe DC field, between 10 K and 320 K. M vs H data were also collected at 50 K and 300 K, sweeping fields from +10,000 Oe to -10,000 Oe.

Results and Discussion

The three-dimensional assembly of discrete nanoparticles of Fe_{2-x}Ni_xP is based on the methodologies developed by the Brock group for InP and Ni₂P nanoparticle assemblies, with minor modifications.^{39, 40} The Fe_{2-x}Ni_xP nanoparticles (target x = 0.8) were synthesized by published methods and found to be iron-rich relative to the target composition (x ranging from 0.6-0.7, depending on the batch).⁷ The particles were thiolate exchanged using a ligand with pendant carboxylate (11-MUA) or methyl group (1-DDT), and assembled using 3% H₂O₂ as an oxidant. The wet gels were aged for two weeks and supercritically dried to obtain Fe_{2-x}Ni_xP aerogels.

Gelation of Discrete MUA-capped Fe_{2-x}Ni_xP Nanoparticles with Different Aspect Ratios

The size and the shape of Fe_{2-x}Ni_xP (0<x<2) nanoparticles are composition-dependent, with a tendency to form rods when x≤0.8. Tunability of the aspect ratio has been reported by varying the volume of TOP in the reaction,⁷ but we find that oleylamine also plays a role in dictating the length (L) and width (W) of the rods as shown in **Figure 1 (a-c)** and **Figure S1.** Short rods of Fe_{2-x}Ni_xP nanoparticles were synthesized using 3.0 mL of TOP and 2.0 mL of oleylamine (L: 18.83 \pm 2.50 nm, W:11.3 \pm 1.09 nm and aspect ratio, AR = 1.7). Increasing the TOP to 5 mL while using the same amount of oleylamine, increased the length of the nanorod by about 1.5x (L: 29.50 \pm 10.50 nm) and decreased the width by about 20% (W: 9.10 \pm 1.01 nm) nearly doubling the aspect ratio (AR = 3.2). Subsequently decreasing the oleylamine amount to 1.0 mL and keeping the TOP amount unchanged at 5.0 mL produced rods of intermediate size (L: 20.12 \pm 2.30 nm, W: 7.48 \pm 0.87 nm, AR = 2.7; **Figure S1**)

These nanorods of different aspect ratio were then assembled into 3-D architectures by the oxidation-induced sol-gel method. Briefly, the nanoparticles were thiolate exchanged with 11-MUA and then 3%(v/v) H₂O₂ was added as the oxidant into the purified nanoparticle dispersion in ethanol to induce gelation. After supercritical drying, a solid black monolith was obtained in each case (insets: Figure 1 (d-f)). These monoliths comprise an interconnected network morphology with an extensive network of pores across a range of sizes (Figure 1 (d-f)). Figure 2 shows the PXRD patterns of discrete nanoparticles and the corresponding aerogel, relative to Figure 1. According to the Scherrer size calculations it is evident that the crystallite size computed from the (111) reflection decreases by 10-25 % upon aerogel formation (Table S1). This we attribute to surface etching and/or conversion of surface crystalline phosphide to amorphous oxide (phosphite/ate).

This "shrinking" is also evident in the TEM. An assessment of ca 20 NRs visible at edges of the gels revealed a notable decrease in the length of the rods from 15-35%, with the greater changes seen for the longer rods. Changes in width were minimal, with all samples having cross-sectional diameters of ca 8 nm. When the width and length changes are combined, it becomes clear that the aspect ratios are quite similar in the three gel samples: 1.8, 2.1, and 2.3, despite being quite different in the starting nanoparticles (1.7, 2.7, and 3.2). These data are consistent with preferential etching on the tips of the nanorods.

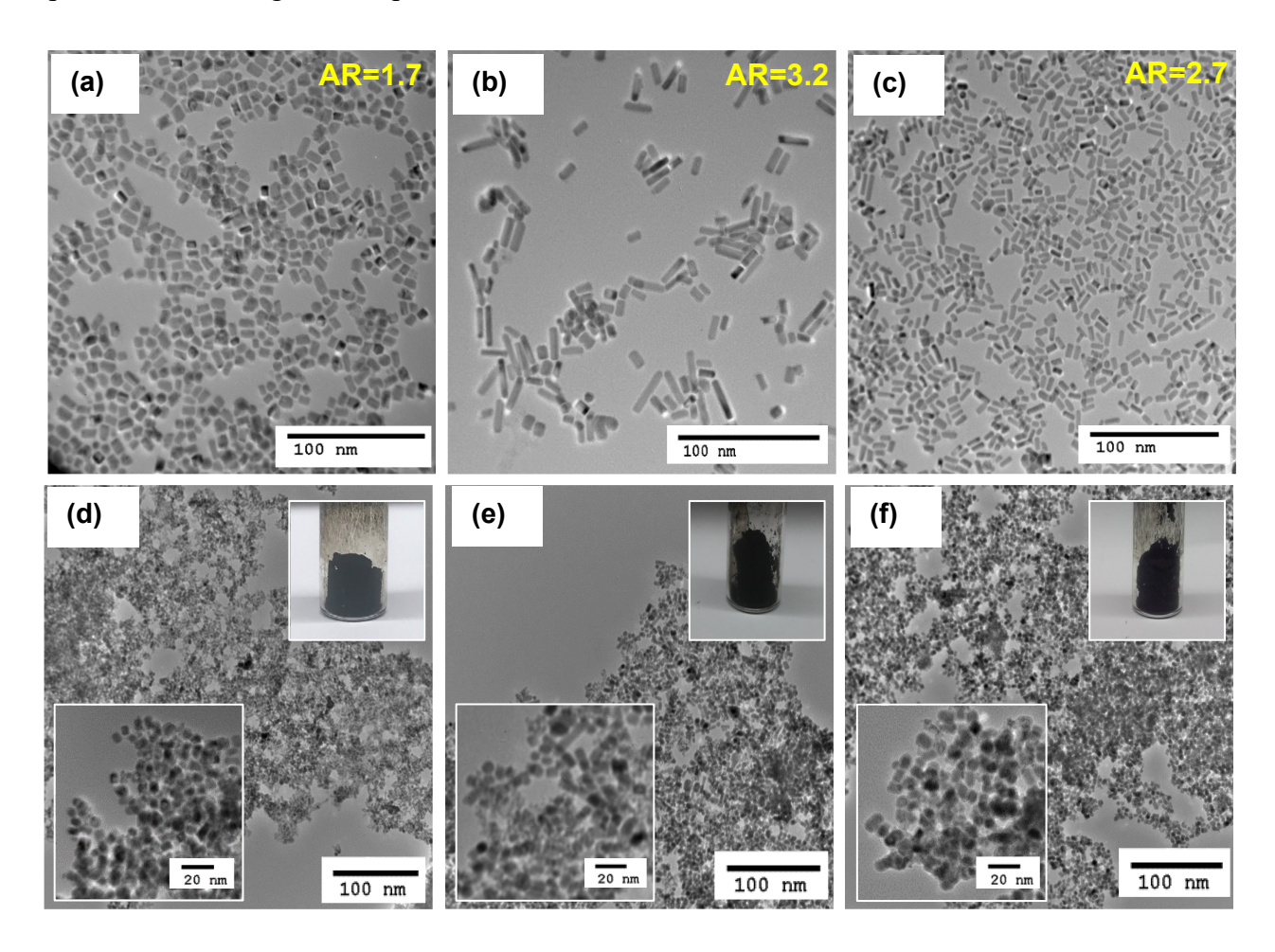


Figure 1: TEM images of $Fe_{2-x}Ni_xP$ (target x = 0.8) nanoparticles/nanorods (a-c) before and (d-f) after 3-D assembly (thiolate exchanged with 11-MUA). The inset on each image shows the corresponding monoliths obtained after supercritical drying of the 3-D assemblies and high magnification TEM images

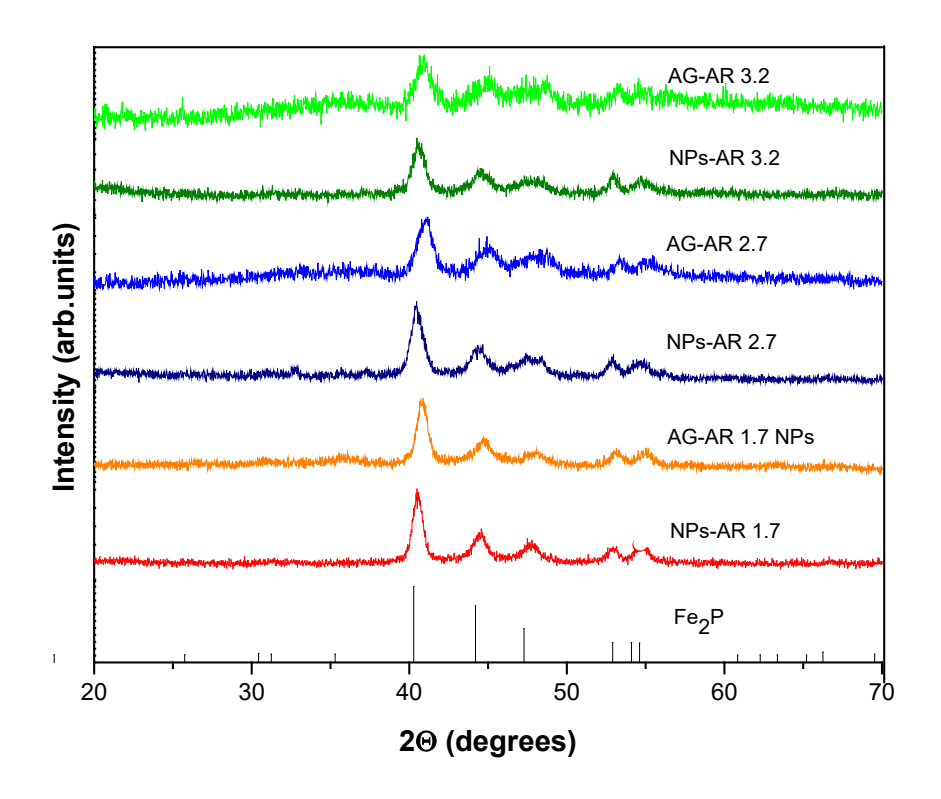


Figure 2: The PXRD patterns of thiolate-capped (11-MUA) nanoparticles (NPs) of $Fe_{2-x}Ni_xP$ (targeting x = 0.8) with differing aspect ratios (ARs) and the resultant aerogels (AGs) produced by oxidative assembly. Fe_2P and Ni_2P adopt the same structure type and have similar lattice parameters. As the targeted compositions are Fe-rich, the reference pattern of Fe_2P from the ICDD database (PDF # 00-051-0943) is shown for comparison. Slight shifts to higher 2 Θ for the gels are an artifact of the PXRD sample holder.

In order to probe the porosity of the aerogels, nitrogen physisorption data were acquired as shown in **Figure 3**. The adsorption-desorption isotherms of all three assemblies are similar in shape and represent a type IV curve, characteristic of a mesoporous (2-50 nm pore diameter) material. The surface areas computed from the Brunauer-Emmett-Teller (BET) model are similar for aerogels produced from the NPs with aspect ratios of AR = 1.7, 4.7 at 86-89 m²/g, whereas the intermediate AR = 2.7 sample has a notably larger surface area (107 m²/g).

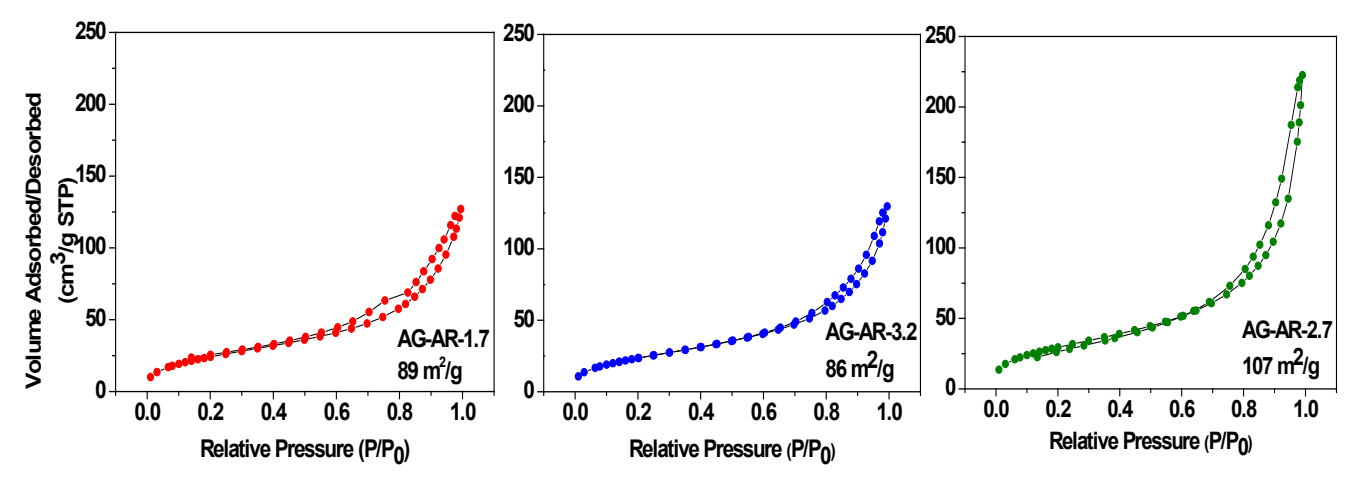


Figure 3: Nitrogen adsorption/desorption isotherms of aerogels prepared from $Fe_{2-x}Ni_xP$ (target x = 0.8) nanorods of aspect ratios 1.7, 4.7, and 2.7.

To better understand the chemical changes occurring during the gelation process, XRF analyses were done on starting NPs of AR = 1.8-2.0, MUA ligand exchanged NPs, and the resultant aerogel. The results are shown in **Table S2**. Despite targeting a composition of Fe_{1.2}Ni_{0.8}P, the asprepared NPs were slightly Fe-rich and sub-stoichiometric in phosphorus, with a composition of Fe_{1.34}Ni_{0.66}P_{0.95}. Upon MUA ligand exchange, the metal ratios are essentially unchanged, but P is even more sub-stoichiometric, Fe_{1.31}Ni_{0.69}P_{0.86} which may reflect loss of surface TOP ligands during the ion-exchange process. The MUA aerogels retain the Fe 1.3: Ni 0.7 metal ratio, but are now super-stoichiometric in P (**Table S2**): Fe_{1.27}Ni_{0.73}P_{1.18}. As there is no source of additional phosphorus, this super-stoichiometry must arise from metal losses during the oxidative assembly process. As the metal ratio is unchanged, the dissolution rates for the two metals must be comparable.

As mentioned in the introduction, oxidation-induced assembly on phosphide particles ligated with groups having chelating pendant functionalities can give rise to a combination of olation linkages (due to ligand stripping) and metal-ion crosslinking (due to liberation of metal

cations during ligand stripping, and subsequent crosslinking of remaining surface ligands). As a means to ensure no metal-ion crosslinking, we prepared a new batch of nanoparticles targeting the same composition (x = 0.8) and aspect ratio nanoparticles (AR = 1.7, synthesized using 2.0 mL oleylamine and 5.0 mL TOP), and capped it with 1-DDT. Unlike 11-MUA, 1-DDT has no pendent carboxylate group, as in 11-MUA, although the chain length is the same. Because of batch-to-batch variability, the resultant nanorods had a slightly larger aspect ratio (AR = 1.9) (see **Figure S2**) but the composition was unchanged (**Table S2**). Treating the DDT-capped particles with H_2O_2 led to gelation. After aging for two weeks, the gel was supercritically dried to produce a black monolith with a composition of $Fe_{1.34}Ni_{0.66}P_{1.19}$, as obtained from XRF (**Table S2**). As was noted for the MUA AG, the DDT AG has the same metal ratio as precursor particles and is superstoichiometric in P (metal: P ratio = 2: 1.2) indicative of non-selective metal etching in the oxidative assembly process (**Table S2**). The TEM image of this aerogel is shown in **Figure 4** (a) and the PXRD patterns of the original nanoparticles and aerogel is shown in **Figure 4** (b).

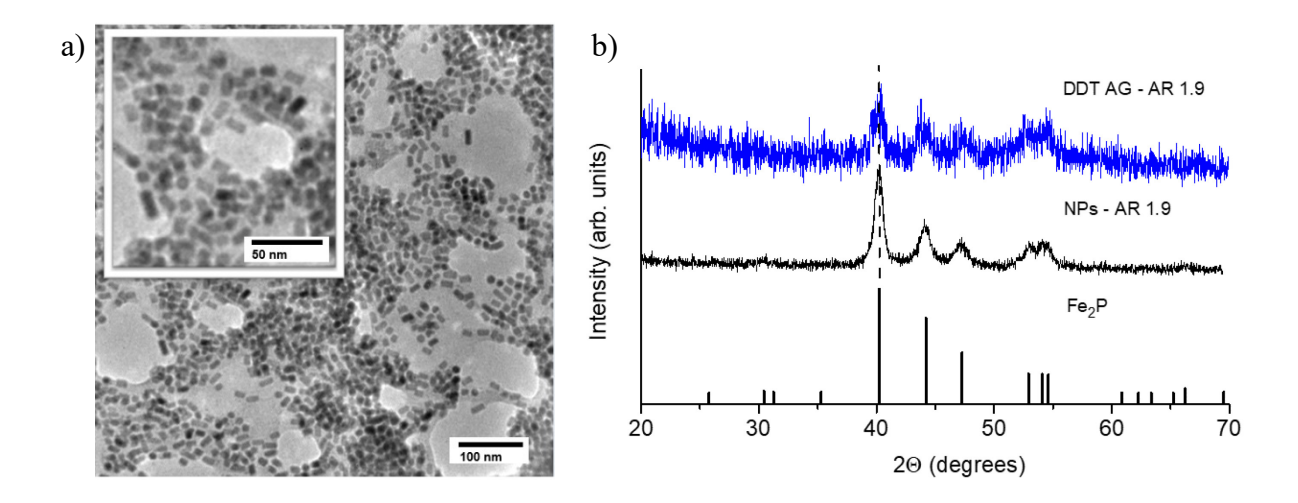


Figure 4: (a) TEM image of the $Fe_{1.3}Ni_{0.7}P$ aerogel produced by oxidative assembly of 1-DDT-capped NPs (AR = 1.9); (b) PXRD pattern of the 1-DDT-capped nanoparticles and resultant aerogel.

As revealed by the TEM, the monolith is composed of an interconnected network of nanoparticles, but unlike the case for the gel produced from MUA-capped nanorods, the particles appear to be encased in an amorphous matrix, which may be associated with formation of phosphite/ate upon oxidation of surface phosphide. The Scherrer size calculation of the crystallite size of the original nanoparticles is *ca.* 13 nm and this increases slightly in the aerogel to *ca.* 14 nm. It is worth noting that the initiation of gelation of 1-DDT-capped nanoparticles takes much longer compared to 11-MUA-capped nanoparticles, (12 h vs. 1 h), and forms a much weaker monolith. This may be associated in part with the hydrophobicity of the DDT ligands slowing the oxidation process. Attempts to conduct surface area measurement of this sample were not successful due to excessive out-gassing. This may be associated with a reduction of accessible pores due to occlusion with amorphous phosphite/ate. 48

To better understand the how the gelation process affects the surface chemistry of the AG, and find confirmatory evidence of phosphorus oxidation to support the hypothesis that phosphite/phosphate olation is responsible for gelation of DDT-NPs, and assess whether this also contributes to gelation of MUA-NPs, we performed XPS analysis of the as-prepared NPs, the MUA AG and the DDT AG (See **Figure S3** and **Table S3**). In all three samples, two phosphorus peaks are observed, one centered close to a binding energy of 129 eV attributed to P in the metal phosphide, and one at 133 eV that corresponds to "oxidized" P. In the case of the NPs, the peak at 133 eV could be due to either oxidation of surface phosphide (to phosphite/ate) or bound trioctylphosphine oxide from oxidation of TOP in the synthesis. In the AG samples, this peak is almost certainly due to amorphous phosphate or phosphite from the oxidation-induced gelation. It is extremely challenging to distinguish between phosphine oxide, phosphite, and phosphate, by XPS as the binding energy ranges for these different species all overlap. Surprisingly, the relative

peak areas for the peaks at 129 and 133 eV are constant for the NP, MUA AG, and DDT AG samples, such that one third of the P is present in the reduced form and two-thirds of the P is oxidized. This is distinct from our prior work on Ni₂P gels, where there was a clear decrease in the ratio of reduced to oxidized P after gelation with hydrogen peroxide.⁴⁰ Given the absence of any new phases in the PXRD pattern, we expect the oxidized phosphorous is amorphous in nature.

As another means to assess the role of different mechanisms driving gelation in 11-MUA and 1-DDT capped Fe_{1.3}Ni_{0.7}P nanoparticles, and consequently, different inter-particle linkages, we probed the stability of the gels towards dispersion with EDTA. 49,50 Gelation associated with metal-ion crosslinking between pendant carboxylate functionalities on 11-MUA should be reversed in the presence of EDTA due to sequestration of the crosslinking ions by EDTA chelation; whereas gelation arising solely from olation of phosphite/ate (i.e., employing 1-DDT, with no chelating pendant groups) should not be affected by introduction of EDTA. As shown in **Figure** 5, when a pH = 12 solution of EDTA was introduced drop-wise to the aerogels prepared from 11-MUA and 1-DDT capped nanoparticles, the aerogel prepared from 11-MUA capped particles exhibited partial dispersion (Figure 5 (a)), and within 5 minutes a black residue had settled out and a wine-red supernatant was evident (Figure 5 (b)). To better understand the change in color of the EDTA solution after reaction with the aerogel produced from MUA-capped particles, we prepared a series of solutions containing EDTA plus Fe(III) and/or Ni(II) along with MUA (see Figure S4). The red color is best associated with Fe(III), although a combination of Fe(III) and Ni(II) cannot be ruled out. These data suggest that there are metal ions outside the phosphide core, likely tethered to pendant carboxylates and reinforcing the phosphite/phosphate network anticipated from hydrogen peroxide oxidation of phosphide. In contrast, the aerogel produced from DDT-capped particles did not disperse when EDTA was added and the EDTA remains colorless

(**Figure 5 (c)**) despite agitation. A control reaction with the starting NPs also did not show any color change over the course of an hour, suggesting that labile metal ions are not present in either sample (**Figure S5**). While limited wetting due to the hydrophobic surface ligands could be a problem, we note that if left long enough (overnight), nanoparticles will start to dissolve, suggesting the EDTA is not only capable of wetting the surface, but eventually sequestering bound metal ions.

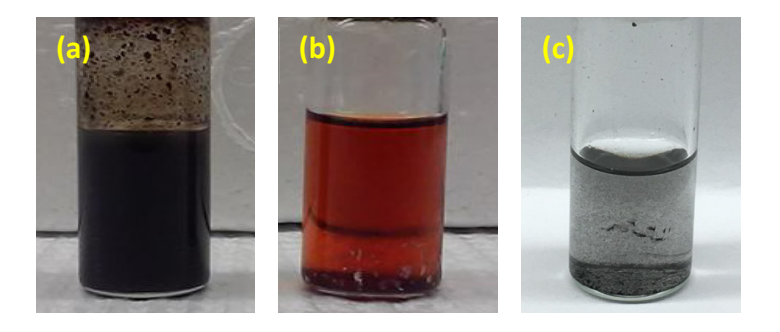


Figure 5: (a) About 1 min after EDTA addition into Fe_{1.3}Ni_{0.7}P + 11-MUA aerogel; (b) supernatant of sample in a; (c) EDTA addition into Fe_{1.3}Ni_{0.7}P +1-DDT aerogel

Analogous to our results obtained with Ni₂P, we presume that 1-DDT, which does not have a pendent carboxylate capable of metal-crosslinking results in phosphite/ate linkages from oxidation of phosphides. As a means to probe this hypothesis, we evaluated the stability of the network to high temperature reduction relative to 11-MUA-capped particles. Phosphates of the middle-to-late first row transition metals (post Mn) undergo reduction to phosphide under temperature programmed reduction conditions. Prior work has established 400 °C under forming gas to be sufficiently reducing to convert surface phosphate to phosphide for nanoparticles of Ni₂P and Ni_{2-x}M_xP (M = Co, Fe). 51-53 Indeed, this is a standard process for activation of supported phosphide catalysts passivated in oxygen. 54, 55 We reasoned that the chemical transformation would eliminate the interparticle phosphate linkages and cleave the network. Our prior work on

MUA-capped Ni_2P oxidized with H_2O_2 , or intentionally crosslinked with Ni^{2+} , revealed the network to be stable to carbothermal reduction up to 400 °C (in situ TEM studies conducted on a carbon-coated grid).⁴⁰

The aerogels prepared from 1-DDT capped nanoparticles were heated for 1 h under 5% H_2 at 400 °C. **Figure 6** shows the TEM image and PXRD relevant to the original gel and the aerogel heat treated under reducing conditions. According to **Figure 6** (a), the TEM image indicates breaking up of the extended network into aggregated small pieces and free individual nanoparticles (compare to **Figure 4** (a)). These individual nanoparticles are more common in the grid areas analyzed by TEM, than are the aggregates, consistent with interparticle cleavage upon reduction of phosphite/ate to phosphide. In addition, we also noted subtle changes in crystallite size $(13.0\pm0.1 \text{ nm} \text{ to } 12.0\pm0.2 \text{ nm})$ and the aspect ratio (1.7 to 1.6) after heat treatment. Finally, while we did not specifically evaluate the samples for sulfidation due to decomposition of thiolate ligands, we think it unlikely given that transition metal phosphides (M_2P) are excellent hydrodesulfurization catalysts because they release sulfur under reducing conditions (in contrast to metals). ⁵⁶

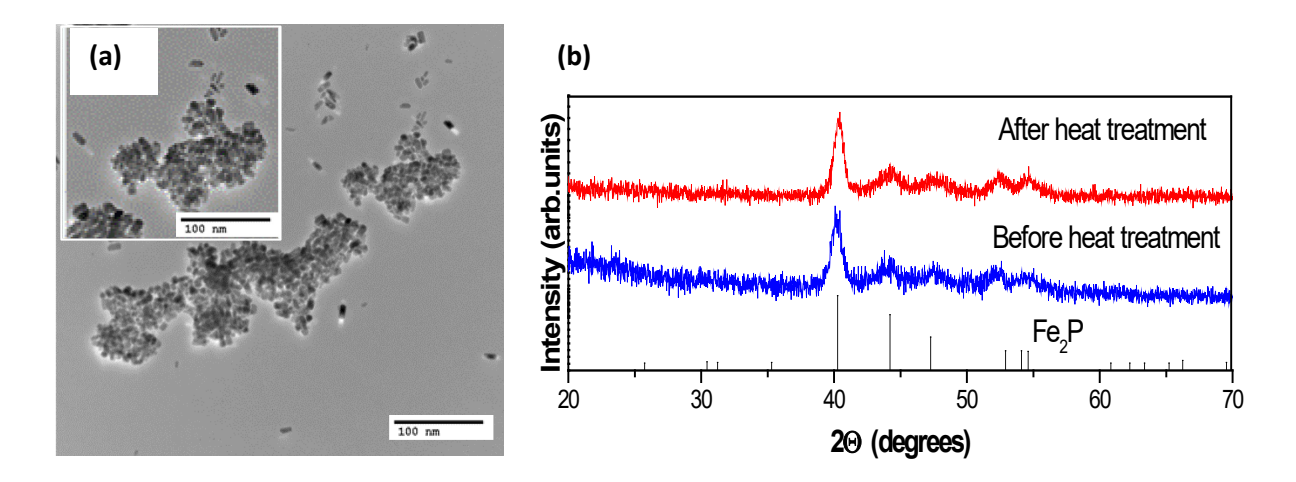


Figure 6: AG prepared from 1-DDT-capped $Fe_{1.3}Ni_{0.7}P$ NPs of AR = 1.7 nanorods treated under reducing conditions (5% H_2) at 400 °C for 1 h (a) TEM image and (b) PXRD data. The inset shows a magnified view

In comparison, **Figure 7** shows consequences of heating towards the aerogels prepared from 11-MUA-capped particles under forming gas at 400 °C. From the TEM images it is observed that the aerogel is largely intact, in contrast to the DDT AG sample. However, the network has undergone significant compaction, resulting in a decrease in surface area by ca 50% (see Figure S6). Moreover, we also noted subtle changes in crystallite size (12.0±0.2 nm to 11.0±0.1 nm) and the aspect ratio (1.7 to 1.6) after heat treatment.

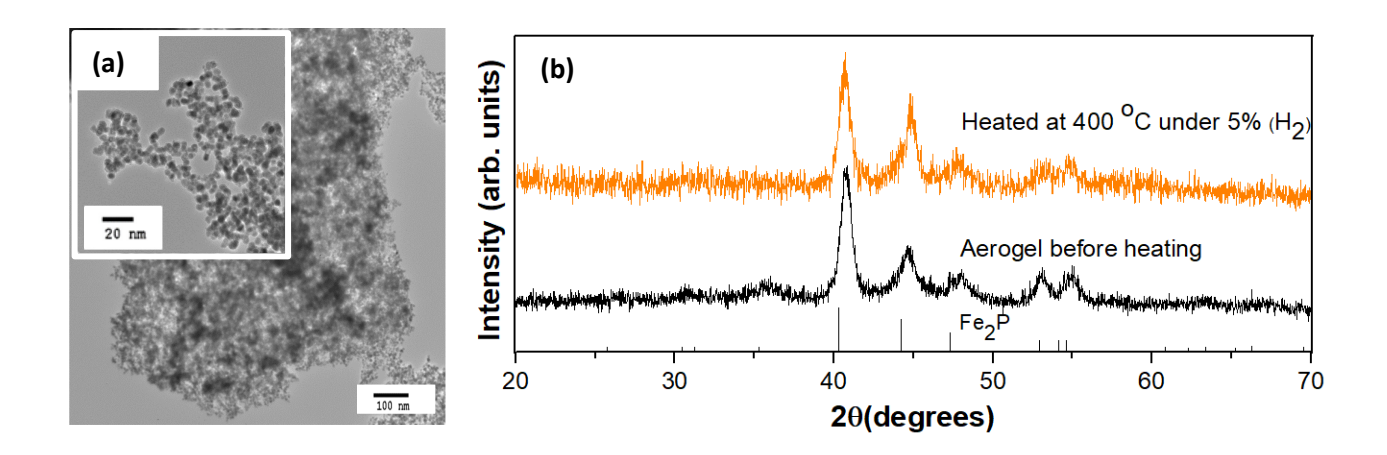


Figure 7: AG prepared from 11-MUA-capped $Fe_{1.3}Ni_{0.7}P$ AR = 1.7 nanorods treated under reducing conditions (5% H_2) at 400 °C for 1 h (a) TEM image and (b) PXRD data. The inset shows the enlarged TEM image of the gel network

Magnetic Measurements of 3-D Assembled Aerogels:

In order to evaluate the magnetic properties, three samples of Fe_{1.3}Ni_{0.7}P nanoparticles with an aspect ratio of 1.8-2.0 were synthesized. Two of the synthesized nanoparticles samples were then thiolate exchanged separately by 11-MUA and 1-DDT. As shown in **Table S2**, the metal

ratios for the three NP samples are essentially the same, whereas the P is slightly substoichiometric relative to metal content in the as-prepared NPs, and more so after ligand exchange, a possible indication of displacement of surface phosphine/phosphine oxide by thiolate. Oxidation-induced sol-gel methods were then employed to assemble thiolate functionalized nanoparticles into aerogel networks. **Figure S7** shows the PXRD data of the starting nanoparticles and resultant gels; the corresponding TEM data for comparable particles ligand exchanged with MUA and DDT is shown in **Figure S8**; the corresponding TEM data for the gels is shown in **Figure S9**. Characterization of the resulting gels by XRF suggested no significant change in the Fe/Ni ratio relative to the starting NPs; however, P is now super-stoichiometric, with a metal-to-P ratio of 2:1.2 (**Table S2**). These data suggest that the process of gelation has resulted in some overall metal dissolution, presumably by surface etching during the oxidation process. As the Fe/Ni ratio is not affected, the dissolution presumably occurs at comparable rates for the two metals.

The temperature (T) dependence of the magnetization (M) was measured under zero-field-cooled (ZFC) and field-cooled (FC) conditions in the range 10-300 K under an external magnetic field of 100 Oe for all samples (**Figure 8**). In addition to ZFC and FC measurements, field (H) dependent magnetization was probed at 50 K and 300 K, between -10,000 and +10,000 Oe for each sample (**Figure 9**, **Figure S10**). In order to make meaningful comparisons among the different samples, the metal content was quantified by ICP-MS and the magnetic data are normalized to moles of metal (Fe + Ni). As shown in **Table S2**, the imputed mass % of Fe_{1.3}Ni_{0.7}P in the starting NPs, MUA AG and DDT AG was comparable for all the samples, ranging from 52-58%. The remainder is attributed to surface ligands and oxide formation.

Single-domain magnetic nanoparticles are characterized by a blocking temperature, T_B, that reflects the highest temperature at which coercivity is retained in the magnetization vs. field

data (the transition from the blocked state to the superparamagnetic state). Below this temperature, ramping the field positive and negative results in hysteresis, such that at zero applied field, the sample retains some residual magnetization (M_r) and an additional field (the coercive field, H_c) is required to bring the magnetization to zero. At high fields, the sample becomes fully ordered and saturation is achieved, with the magnetic saturation (M_s) reflecting the ferromagnetic moment. Above T_B , the sample is superparamagnetic; it continues to saturate at high field, but the magnetization is able to relax on the time-scale of the measurement, so no coercivity is observed. The magnitude of T_B has a positive dependence on the intrinsic magnetocrystalline anisotropy energy of the material and on extrinsic factors of size and shape, with shape-dependence particularly important when the long-axis aligns with the easy magnetic axis. T_B is identified by a cusp in the temperature-dependent magnetization data acquired after cooling the sample under zero field (zero-field-cooled, ZFC). Ideally (i.e., for samples with narrow size/shape polydispersity), this cusp intersects with magnetization vs. temperature data acquired after cooling under a small applied field (field-cooled, FC; ca. 100 Oe).⁵⁷

Magnetization vs. temperature data are plotted in **Figure 8** for $Fe_{2-x}Ni_xP$ NPs and aerogels prepared from MUA- and DDT-capped precursor NPs. All samples exhibit a cusp in the ZFC data attributed to T_B ; T_B for NPs and MUA-AG samples is near 35 K whereas for DDT-AG $T_B \sim 40$ K. For the NPs, the FC curve nearly overlaps with the ZFC data for $T>T_B$, whereas for the two AG samples, the intersection occurs at a slightly higher temperature, ca 80K. T_B values for the DDT-and MUA- capped aerogels are comparable to the nanoparticle sample in this study, and are in alignment with the T_B values reported by Hitihami-Mudiyanselage *et al.* for nanoparticles of similar composition and aspect ratio.⁷ Likewise, the estimated T_C of ~ 225 K (where the magnetization curve drops to near zero) is consistent with an Fe-rich $Fe_{2-x}Ni_xP$ phase ($x \leq 0.8$).

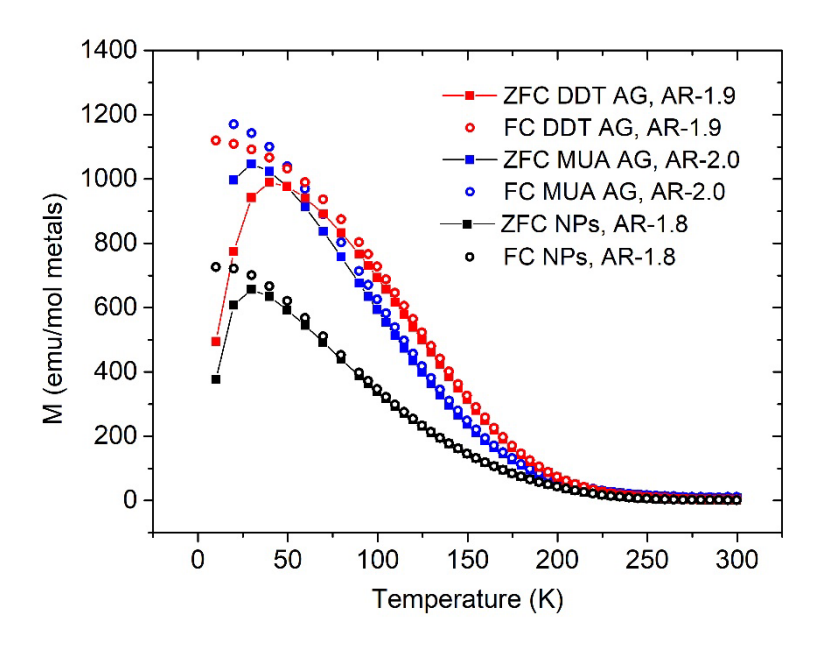


Figure 8: ZFC and FC curves of Fe_{1.4}Ni_{0.6}P, AR=1.8 nanoparticles (NPs), 11-MUA capped Fe_{1.3}Ni_{0.7}P, AR=2.0 aerogels (AG), and 1-DDT capped Fe_{1.3}Ni_{0.7}P, AR=1.9 aerogels. H=100 Oe.

A key difference in between the NPs and AGs is in the magnitude of the molar susceptibility at T_B , which decreases in the order MUA-AG > DDT-AG>> NPs. The enhanced molar moment is also reflected in the Magnetization vs. Field data (M vs. H) at 50 K as an increase in M_s for the AGs relative to the NPs: M_s = 2624, 3171, and 2979 emu/mol metals for NPs, DDT-AG, and MUA-AG, respectively (**Figure 9**). The differences are subtle, but do suggest that the surface chemistry that occurs during the process of assembly has enhanced the magnetic moment of the individual building blocks, whereas we had expected a diminution due to etching. Because data is acquired above T_B , we expected the H_c to be \sim 0; however, as shown in the inset to **Figure 9**, the actual values are all \sim 10 Oe. The residual coercivity likely reflects a distribution in T_B that reflects the intrinsic polydispersity of the sample (standard deviation in size \sim 15%). Overall, there are no distinguishable variations in the magnetic data for AGs vs. NPs that cannot be otherwise attributed natural distributions in particle size/composition arising from the synthetic

methodology. Accordingly, the data suggests that the magnetic behavior of the Fe_{0.7}Ni_{0.3}P aerogels represents the sum of the individual Fe_{0.7}Ni_{0.3}P pHparticles.

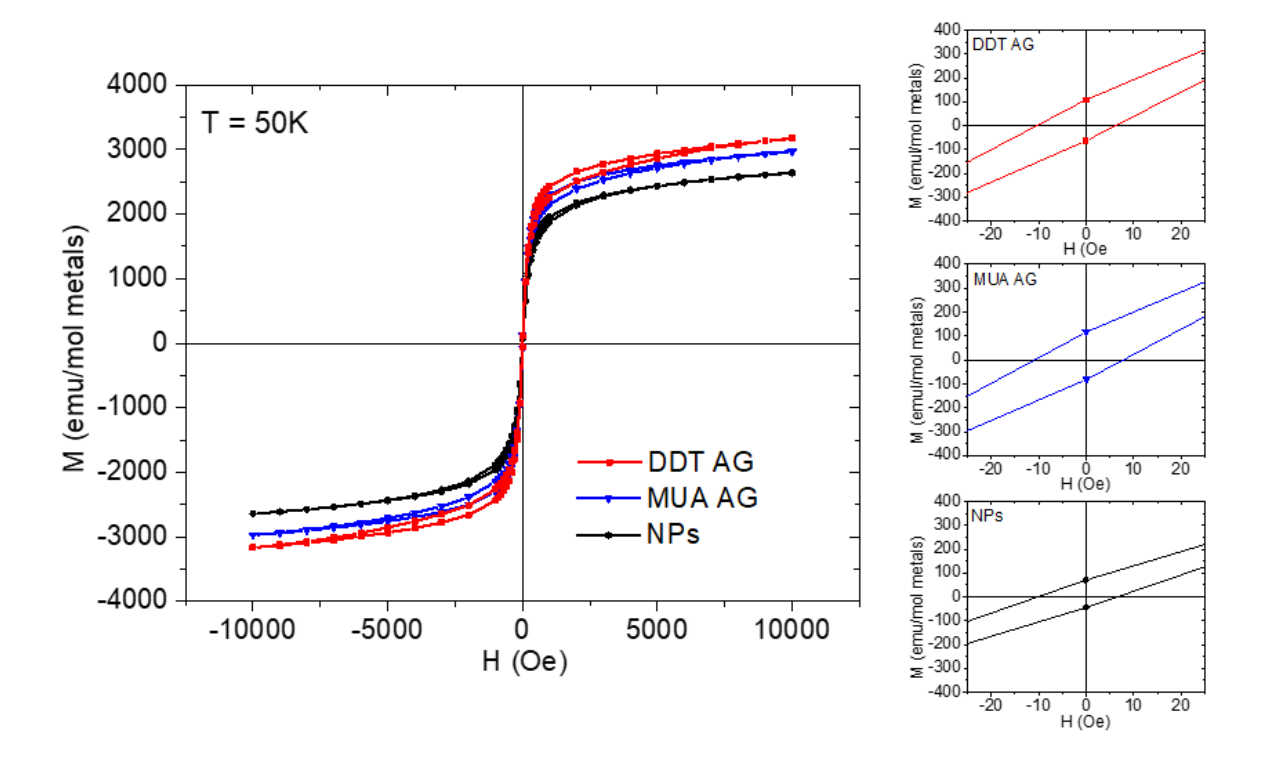


Figure 9: Magnetization (M) of Fe_{1.3}Ni_{0.7}P, AR=1.8 nanoparticles (NPs), MUA capped Fe_{1.3}Ni_{0.7}P, AR=2.0 aerogels (AG), and DDT capped Fe_{1.3}Ni_{0.7}P, AR=1.9 aerogels as a function of applied field (H) at 50 K. The insets show enlarged images near H_C of the hysteresis curves for each sample obtained at 50 K

Conclusions

In the present work we have shown that oxidation-induced assembly of magnetic phosphide nanoparticles can be used to form 3-D integrated pore-matter networks that retain the native properties of the individual components, regardless of the nature of the interparticle interfaces. These data suggest that development of magnetic nanoparticles for applications that benefit from 3-D magnetic pore-matter architectures, such as magnetic refrigeration, can proceed in parallel with work focused on tuning the network density and strength. As a broader impact, this work

opens the door for the assembly of other metal phosphide nanorod materials that have shown unique properties for catalytic applications.^{58, 59}

ASSOCIATED CONTENT

Supporting Information

Figures of size distribution histograms of Fe_{2-x}Ni_xP nanoparticles (NPs) and aerogels (AGs) depicted in Figure 2; TEM image of precursor NPs used to make DDT-AGs shown in Figure 4; XPS spectra of NPs and AGs; photograph of solutions prepared from EDTA, Ni²⁺, Fe³⁺ and MUA for comparison to Figure 5; photos of samples treated with alkaline EDTA, including starting NPs; nitrogen adsorption/desorption isotherms for MUA-AG before and after heating in forming gas; PXRD patterns and corresponding TEM images of NPs, precursor NPs and AGs used in the magnetic analysis; magnetization vs. field data at 300K. Tables of crystallite sizes of NPs and AGs; compositions of NPs, precursor NPs and AG used in the magnetic analysis; contributions of different phosphorus species to the XPS spectrum. This material is available free of charge via the Internet at http://pubs.acs.org.

AUTHOR INFORMATION

Corresponding Author

Stephanie L. Brock—Department of Chemistry, Wayne State University, Detroit, MI 48202, USA; orchid.org/0000-0002-0439-302X; Email: sbrock@chem.wayne.edu

Authors

Malsha A. Hettiarachchi—Department of Chemistry, Wayne State University, Detroit, MI 48202, USA

Tepora Su'a—Department of Chemistry, Wayne State University, Detroit, MI 48202, USA **Ali-hamza Ramzan**—Department of Chemistry, Wayne State University, Detroit, MI 48202, USA

Shiva Pokhrel—Department of Physics and Astronomy, Wayne State University, Detroit, MI 48201, USA

Boris Nadgorny—Department of Physics and Astronomy, Wayne State University, Detroit, MI 48201, USA

Notes

MAH and TS contributed equally to the work. The authors declare no competing financial interest.

ACKNOWLEDGEMENTS

This work was supported by the National Science Foundation (DMR-1904775) This work employed XRF, TEM, and PXRD, all housed in the Lumigen Instrument Center, Department of Chemistry, and PPMS housed in the Magnetic Characterization Facility, Department of Physics, Wayne State University The JEOL-2010 TEM was acquired using funds from NSF grant #0216084, and the PXRD facility is supported by NSF grant #1427926.

REFERENCES

- 1. Kang, Q.; Li, M.; Shi, J.; Lu, Q.; Gao, F., A Universal Strategy for Carbon-Supported Transition Metal Phosphides as High-Performance Bifunctional Electrocatalysts towards Efficient Overall Water Splitting. *ACS Appl. Mater. Interface* **2020**, *12*, 19447-19456.
- 2. Zhao, H.; Wang, Y.; Fang, L.; Fu, W.; Yang, X.; You, S.; Luo, P.; Zhang, H.; Wang, Y., Cation-tunable flower-like $(Ni_xFe_{1-x})_2P@$ graphitized carbon films as ultra-stable electrocatalysts for overall water splitting in alkaline media. *J. Mater. Chem. A* **2019**, *7*, 20357-20368.
- 3. Zhang, B.; Zhang, J.; Tang, X.; Lui, Y. H.; Hu, S., An investigation of Fe incorporation on the activity and stability of homogeneous (Fe_xNi_{1-x})₂P solid solutions as electrocatalysts for alkaline hydrogen evolution. *Electrochim. Acta* **2019**, *294*, 297-303.
- 4. Read, C. G.; Callejas, J. F.; Holder, C. F.; Schaak, R. E., General Strategy for the Synthesis of Transition Metal Phosphide Films for Electrocatalytic Hydrogen and Oxygen Evolution. *ACS Appl. Mater. Interface* **2016**, *8*, 12798-12803.
- 5. Shin, D.; Kim, H. J.; Kim, M.; Shin, D.; Kim, H.; Song, H.; Choi, S.-I., Fe_xNi_{2-x}P Alloy Nanocatalysts with Electron-Deficient Phosphorus Enhancing the Hydrogen Evolution Reaction in Acidic Media. *ACS Catal.* **2020**, *10*, 11665-11673.
- 6. Winkler, N.; Peterlechner, M.; Wilde, G., Controlling crystallization, phase transformation and magnetic properties of amorphous FeNiP by annealing in nano-confinement. *J. Mater. Chem. C* **2015**, *3*, 7543-7551.
- 7. Hitihami-Mudiyanselage, A.; Arachchige, M. P.; Seda, T.; Lawes, G.; Brock, S. L., Synthesis and Characterization of Discrete Fe_xNi_{2-x}P Nanocrystals (0 < x < 2): Compositional Effects on Magnetic Properties. *Chem. Mater.* **2015**, *27*, 6592-6600.
- 8. Yoon, K. Y.; Jang, Y.; Park, J.; Hwang, Y.; Koo, B.; Park, J.-G.; Hyeon, T., Synthesis of uniform-sized bimetallic iron–nickel phosphide nanorods. *J. Solid State Chem.* **2008**, *181*, 1609-1613.
- 9. Franco, V.; Blázquez, J. S.; Ingale, B.; Conde, A., The Magnetocaloric Effect and Magnetic Refrigeration Near Room Temperature: Materials and Models. *Annu. Rev. Mater. Res.* **2012**, *42*, 305-342.

- 10. Romero Gómez, J.; Ferreiro Garcia, R.; De Miguel Catoira, A.; Romero Gómez, M., Magnetocaloric effect: A review of the thermodynamic cycles in magnetic refrigeration. *Renew. Sustain. Energy Rev.* **2013**, *17*, 74-82.
- 11. Brown, G. V., Magnetic heat pumping near room temperature. *J. Appl. Phys.* **1976,** 47, 3673-3680.
- 12. Lozano, J. A.; Kostow, M. P.; Brück, E.; de Lima, J. C.; Prata, A. T.; Wendhausen, P. A. P., Porous manganese-based magnetocaloric material for magnetic refrigeration at room temperature. *J. Magn. Magn. Mater.* **2008**, *320*, e189-e192.
- 13. Lyubina, J.; Schäfer, R.; Martin, N.; Schultz, L.; Gutfleisch, O., Novel Design of La(Fe,Si)₁₃ Alloys Towards High Magnetic Refrigeration Performance. *Adv. Mater.* **2010**, *22*, 3735-3739.
- 14. Moore, J. D.; Morrison, K.; Sandeman, K. G.; Katter, M.; Cohen, L. F., Reducing extrinsic hysteresis in first-order La(Fe,Co,Si)₁₃ magnetocaloric systems. *Appl. Phys. Lett.* **2009**, *95*, 252504.
- 15. Lyubina, J., Recent advances in the microstructure design of materials for near room temperature magnetic cooling (invited). *J. Appl. Phys.* **2011**, *109*, 07A902.
- 16. Lisiecki, I.; Pileni, M.-P., Ordering at Various Scales: Magnetic Nanocrystals. *J. Phys. Chem. C* **2012**, *116*, 3-14.
- 17. Nicolas-Boluda, A.; Yang, Z.; Guilbert, T.; Fouassier, L.; Carn, F.; Gazeau, F.; Pileni, M. P., Self-Assemblies of Fe₃O₄ Nanocrystals: Toward Nanoscale Precision of Photothermal Effects in the Tumor Microenvironment. *Adv. Funct. Mater.* **2021**, *31*, 2006824.
- 18. Yang, Z.; Altantzis, T.; Zanaga, D.; Bals, S.; Tendeloo, G. V.; Pileni, M.-P., Supracrystalline Colloidal Eggs: Epitaxial Growth and Freestanding Three-Dimensional Supracrystals in Nanoscaled Colloidosomes. *J. Am. Chem. Soc.* **2016**, *138*, 3493-3500.
- 19. Lisiecki, I.; Parker, D.; Salzemann, C.; Pileni, M. P., Face-Centered Cubic Supra-Crystals and Disordered Three-Dimensional Assemblies of 7.5 nm Cobalt Nanocrystals: Influence of the Mesoscopic Ordering on the Magnetic Properties. *Chem. Mater.* **2007**, *19*, 4030-4036.
- 20. Kostiainen, M. A.; Ceci, P.; Fornara, M.; Hiekkataipale, P.; Kasyutich, O.; Nolte, R. J. M.; Cornelissen, J. J. L. M.; Desautels, R. D.; van Lierop, J., Hierarchical Self-Assembly and Optical Disassembly for Controlled Switching of Magnetoferritin Nanoparticle Magnetism. *ACS Nano* **2011**, *5*, 6394-6402.
- 21. Majetich, S. A.; Wen, T.; Booth, R. A., Functional Magnetic Nanoparticle Assemblies: Formation, Collective Behavior, and Future Directions. *ACS Nano* **2011**, *5*, 6081-6084.
- 22. Lesnyak, V.; Wolf, A.; Dubavik, A.; Borchardt, L.; Voitekhovich, S. V.; Gaponik, N.; Kaskel, S.; Eychmüller, A., 3D Assembly of Semiconductor and Metal Nanocrystals: Hybrid CdTe/Au Structures with Controlled Content. *J. Am. Chem. Soc.* **2011**, *133*, 13413-13420.
- 23. Milliron, D. J.; Buonsanti, R.; Llordes, A.; Helms, B. A., Constructing Functional Mesostructured Materials from Colloidal Nanocrystal Building Blocks. *Acc. Chem. Res.* **2014**, *47*, 236-246.
- 24. Singh, A.; Lindquist, B. A.; Ong, G. K.; Jadrich, R. B.; Singh, A.; Ha, H.; Ellison, C. J.; Truskett, T. M.; Milliron, D. J., Linking Semiconductor Nanocrystals into Gel Networks through All-Inorganic Bridges. *Angew. Chem. Int. Ed.* **2015**, *54*, 14840-14844.
- 25. Rechberger, F.; Niederberger, M., Synthesis of aerogels: from molecular routes to 3-dimensional nanoparticle assembly. *Nanoscale Horizons* **2017**, *2*, 6-30.
- Wen, D.; Eychmüller, A., 3D assembly of preformed colloidal nanoparticles into gels and aerogels: function-led design. *Chem. Commun.* **2017**, *53*, 12608-12621.

- 27. Matter, F.; Luna, A. L.; Niederberger, M., From colloidal dispersions to aerogels: How to master nanoparticle gelation. *Nano Today* **2020**, *30*, 100827.
- 28. Rusch, P.; Zámbó, D.; Bigall, N. C., Control over Structure and Properties in Nanocrystal Aerogels at the Nano-, Micro-, and Macroscale. *Acc. Chem. Res.* **2020**, *53*, 2414-2424.
- 29. Wolf, A.; Lesnyak, V.; Gaponik, N.; Eychmüller, A., Quantum-Dot-Based (Aero)gels: Control of the Optical Properties. *J. Phys. Chem. Lett.* **2012**, *3*, 2188-2193.
- 30. Gaponik, N.; Herrmann, A.-K.; Eychmüller, A., Colloidal Nanocrystal-Based Gels and Aerogels: Material Aspects and Application Perspectives. *J. Phys. Chem. Lett.* **2011**, *3*, 8-17.
- 31. Gaponik, N.; Wolf, A.; Marx, R.; Lesnyak, V.; Schilling, K.; Eychmüller, A., Three-Dimensional Self-Assembly of Thiol-Capped CdTe Nanocrystals: Gels and Aerogels as Building Blocks for Nanotechnology. *Adv. Mater.* **2008**, *20*, 4257-4262.
- 32. Mohanan, J. L.; Arachchige, I. U.; Brock, S. L., Porous Semiconductor Chalcogenide Aerogels. *Science* **2005**, *307*, 397-401.
- 33. Arachchige, I. U.; Brock, S. L., Sol-Gel Assembly of CdSe Nanoparticles to Form Porous Aerogel Networks. *J. Am. Chem. Soc.* **2006**, *128*, 7964-7971.
- 34. Arachchige, I. U.; Brock, S. L., Sol-Gel Methods for the Assembly of Metal Chalcogenide Quantum Dots. *Acc. Chem. Res.* **2007**, *40*, 801-809.
- 35. Yu, H.; Brock, S. L., Effects of Nanoparticle Shape on the Morphology and Properties of Porous CdSe Assemblies (Aerogels). *ACS Nano* **2008**, *2*, 1563-1570.
- 36. Ganguly, S.; Brock, S. L., Toward nanostructured thermoelectrics: synthesis and characterization of lead telluride gels and aerogels. *J. Mater. Chem.* **2011**, *21*, 8800-8806.
- 37. Yao, Q.; Brock, S. L., Porous CdTe Nanocrystal Assemblies: Ligation Effects on the Gelation Process and the Properties of Resultant Aerogels. *Inorg. Chem.* **2011**, *50*, 9985-9992.
- 38. Kalebaila, K. K.; Brock, S. L., Lead Selenide Nanostructured Aerogels and Xerogels. *Z. anorganische allgemeine Chem.* **2012**, *638*, 2598-2603.
- 39. Hitihami-Mudiyanselage, A.; Senevirathne, K.; Brock, S. L., Assembly of Phosphide Nanocrystals into Porous Networks: Formation of InP Gels and Aerogels. *ACS Nano* **2013**, *7*, 1163-1170.
- 40. Hitihami-Mudiyanselage, A.; Senevirathne, K.; Brock, S. L., Bottom-Up Assembly of Ni₂P Nanoparticles into Three-Dimensional Architectures: An Alternative Mechanism for Phosphide Gelation. *Chem. Mater.* **2014**, *26*, 6251-6256.
- 41. Gribanov, I. F.; Golovchan, A. V.; Varyukhin, D. V.; Val'kov, V. I.; Kamenev, V. I.; Sivachenko, A. P.; Sidorov, S. L.; Mityuk, V. I., Magnetic and magnetocaloric properties of the alloys $Mn_{2-x}Fe_xP_{0.5}As_{0.5}$ ($0 \le x \le 0.5$). Low Temperature Phys. **2009**, 35, 786-791.
- 42. Shah, N.; Rehan, T.; Li, X.; Tetik, H.; Yang, G.; Zhao, K.; Lin, D., Magnetic aerogel: an advanced material of high importance. *RSC Adv.* **2021**, *11*, 7187-7204.
- 43. Long, J. W.; Logan, M. S.; Carpenter, E. E.; Rolison, D. R., Synthesis and Characterization of Mn-FeO_x Aerogels with Magnetic Properties. *J. Non.-Cryst. Solids* **2004**, *350*, 182-188.
- 44. Long, J. W.; Logan, M. S.; Rhodes, C. P.; Carpenter, E. E.; Stroud, R. M.; Rolison, D. R., Nanocrystalline Iron Oxide Aerogels as Mesoporous Magnetic Architectures. *J. Am. Chem. Soc.* **2004**, *126*, 16879-16889.

- 45. Carpenter, E. E.; Long, J. W.; Rolison, D. R.; Logan, M. S.; Pettigrew, K.; Stroud, R. M.; Kuhn, L. T.; Hansen, B. R.; Mørup, S., Magnetic and Mössbauer spectroscopy studies of nanocrystalline iron oxide aerogels. *J. Appl. Phys.* **2006**, *99*, 08N711.
- 46. Willey, R. J.; Noirclerc, P.; Busca, G., Preparation and Characterization of Magnesium Chromite and Ferrite Aerogels. *Chem. Engin. Commun.***1993**, *123*, 1-16.
- 47. Janulevicius, M.; Klimkevičius, V.; Mikoliunaite, L.; Vengalis, B.; Vargalis, R.; Sakirzanovas, S.; Plausinaitiene, V.; Zilinskas, A.; Katelnikovas, A., Ultralight Magnetic Nanofibrous GdPO₄ Aerogel. *ACS Omega* **2020**, *5*, 14180-14185.
- 48. Pawsey, S.; Kalebaila, K. K.; Moudrakovski, I.; Ripmeester, J. A.; Brock, S. L., Pore Structure and Interconnectivity of CdS Aerogels and Xerogels by Hyperpolarized Xenon NMR. *J. Phys. Chem. C* **2010**, *114*, 13187-13195.
- 49. Lesnyak, V.; Wolf, A.; Dubavik, A.; Borchardt, L.; Voitekhovich, S. V.; Gaponik, N.; Kaskel, S.; Eychmüller, A., 3D Assembly of Semiconductor and Metal Nanocrystals: Hybrid CdTe/Au Structures with Controlled Content. *J. Am. Chem. Soc.* **2011**, *133*, 13413-13420.
- 50. Lesnyak, V.; Voitekhovich, S. V.; Gaponik, P. N.; Gaponik, N.; Eychmüller, A., CdTe Nanocrystals Capped with a Tetrazolyl Analogue of Thioglycolic Acid: Aqueous Synthesis, Characterization, and Metal-Assisted Assembly. *ACS Nano* **2010**, *4*, 4090-4096.
- 51. Topalian, P. J.; Liyanage, D. R.; Danforth, S. J.; d'Aquino, A. I.; Brock, S. L.; Bussell, M. E., Effect of Particle Size on the Deep HDS Properties of Ni₂P Catalysts. *J. Phys. Chem. C* **2019**, *123*, 25701-25711.
- 52. Danforth, S. J.; Liyanage, D. R.; Hitihami-Mudiyanselage, A.; Ilic, B.; Brock, S. L.; Bussell, M. E., Probing hydrodesulfurization over bimetallic phosphides using monodisperse Ni_{2-x}M_xP nanoparticles encapsulated in mesoporous silica. *Surf. Sci.* **2016**, *648*, 126-135.
- 53. Senevirathne, K.; Burns, A. W.; Bussell, M. E.; Brock, S. L., Synthesis and Characterization of Discrete Nickel Phosphide Nanoparticles: Effect of Surface Ligation Chemistry on Catalytic Hydrodesulfurization of Thiophene. *Adv. Funct. Mater.* **2007**, *17*, 3933-3939.
- 54. Zhang, P.; Sun, Y.; Lu, M.; Zhu, J.; Li, M.; Shan, Y.; Shen, J.; Song, C., High-Loading Nickel Phosphide Catalysts Supported on SiO₂–TiO₂ for Hydrodeoxygenation of Guaiacol. *Energy Fuel* **2019**, *33*, 7696-7704.
- 55. Yang, S.; Liang, C.; Prins, R., Preparation and hydrotreating activity of unsupported nickel phosphide with high surface area. *J. Catal.* **2006**, *241*, 465-469.
- 56. Duan, X.; Teng, Y.; Wang, A.; Kogan, V. M.; Li, X.; Wang, Y., Role of sulfur in hydrotreating catalysis over nickel phosphide. *J. Catal.***2009**, *261*, 232-240.
- 57. Frey, N. A.; Peng, S.; Cheng, K.; Sun, S., Magnetic nanoparticles: synthesis, functionalization, and applications in bioimaging and magnetic energy storage. *Chem. Soc. Rev.* **2009**, *38*, 2532-2542.
- 58. Doan-Nguyen, V. V. T.; Zhang, S.; Trigg, E. B.; Agarwal, R.; Li, J.; Su, D.; Winey, K. I.; Murray, C. B., Synthesis and X-ray Characterization of Cobalt Phosphide (Co₂P) Nanorods for the Oxygen Reduction Reaction. *ACS Nano* **2015**, *9*, 8108-8115.
- 59. Zhang, Y.; Li, N.; Zhang, Z.; Li, S.; Cui, M.; Ma, L.; Zhou, H.; Su, D.; Zhang, S., Programmable Synthesis of Multimetallic Phosphide Nanorods Mediated by Core/Shell Structure Formation and Conversion. *J. Am. Chem. Soc.* **2020**, *142*, 8490-8497.

